This is a repository copy of *Magnetohydrodynamic waves in an asymmetric magnetic slab with different external flows*.

White Rose Research Online URL for this paper:
https://eprints.whiterose.ac.uk/191344/

Version: Published Version

Article:

Magnetohydrodynamic Waves in an Asymmetric Magnetic Slab with Different External Flows

Noémi Kinga Zsámberger[1,2,3] , Carmen M. Sánchez Montoya[1,4], and Róbert Erdélyi[1,5,6]

[1] Solar Physics and Space Plasma Research Centre, School of Mathematics and Statistics, University of Sheffield, Hicks Building, Hounsfield Road, Sheffield, S3 7RH, UK; robertus@sheffield.ac.uk
[2] Department of Physics, University of Debrecen, 1. Egyetem tér, H-4010 Debrecen, Hungary
[3] Doctoral School of Physics, University of Debrecen, Egyetem tér 1., H-4010 Debrecen, Hungary
[4] Faculty of Experimental Science, University of Almería, S/N Carretera Sacramento, E-04120 Almería, Spain
[5] Department of Astronomy, Eötvös Loránd University, 1/A Pázmány Péter sétány, H-1117 Budapest, Hungary
[6] Gyula Bay Zoltán Solar Observatory (GSO), Hungarian Solar Physics Foundation (HSPF), Petőfi tér 3., H-5700 Gyula, Hungary

Abstract

Building on recent studies of the Kelvin–Helmholtz instability (KHI) in the solar atmosphere, we investigate a simple analytical model that can further our understanding of how the presence of bulk flows influences the propagation of magnetohydrodynamic (MHD) waves. Our model builds on a series of recent works on stationary MHD waveguides and looks at a magnetic slab with a density asymmetry, as well as asymmetric background steady flows present in its environment. We obtained approximate solutions to the dispersion relation for the important and applicable limiting cases of a thin or a wide slab, as well as low- and high-β plasmas. We also explored the relation between the angular frequency of trapped MHD waves, the limit for the onset of the KHI, and small parameters describing the flow and density asymmetries. Our analytical investigation is complemented by a numerical analysis for various bulk flow speeds and slab widths. Both these avenues of study reveal that the flow field asymmetry has an important effect on both the cutoff frequencies and the stability of trapped MHD waves in the slab configuration.

1. Introduction

Magnetic fields dominate the solar atmosphere, creating a dynamic and inhomogeneous medium that enables the propagation of a wide range of magnetohydrodynamic (MHD) waves. MHD waves have been predicted to be present in the solar atmosphere since the late 1960s (Uchida 1968; Habbal et al. 1979; Roberts 1981b). They were first imaged in 1998 by TRACE, and since then, both their theoretical and observational studies have entered a new "golden age."

Within the family of studies employing simple geometries to construct a physical model of certain solar atmospheric features, the configuration of a magnetic slab employs Cartesian geometry. In the long history of constructing and improving this model, a first step was investigating one interface in a uniform medium—a good summary of which is given by Roberts (1981a). After that, two interfaces (forming a symmetric slab) with magnetic field only on the inside were studied by Roberts (1981b). Adding magnetic fields outside was the following step, proposed by Edwin & Roberts (1982).

Expanding the scope of traditionally symmetric slab models can be accomplished in several ways. One line of investigation has been keeping each of the regions of the slab system uniform and focusing on waves propagating along the slabs, but introducing various sources of asymmetry into the model. A slab placed in a nonmagnetic, asymmetric environment was studied recently by Allcock & Erdélyi (2017). One avenue for further generalizing slab models is to investigate what happens in an asymmetric magnetic slab, which has been done by Zsámberger et al. (2018, 2021a, 2021). Finally, the model may be further expanded to incorporate multilayered slabs, as Shukhobodskaia & Erdélyi (2018) and Allcock et al. (2019) have described.

When it comes to steady as opposed to static models, there are new physical effects to investigate. First, if we add a steady flow to the equilibrium state of a slab (even a symmetric slab), shearing motions may be caused in the flow, which eventually may lead to the appearance of the Kelvin–Helmholtz instability (KHI). Second, the presence of a bulk background flow shifts the phase speeds and the cutoff speeds of waves that can propagate in a specific waveguide (see, e.g., Nakariakov & Roberts 1995; Terra-Homem et al. 2003). Further consequences of the addition of flows, such as negative-energy wave instabilities or resonant flow instabilities, have also been the subject of extensive study (see, e.g., Taroyan & Ruderman 2011; Ryutova 2015).

The influence of steady flows on wave behavior has been studied in multiple geometries. For a description of these effects in a cylindrical flux tube, see, e.g., Somasundaram et al. (1999) and Terra-Homem et al. (2003). The consequences of the presence of a bulk background flow in a symmetric slab geometry were explored by Nakariakov & Roberts (1995). Further, the study of Barbulescu & Erdélyi (2018) can be considered a natural extension of this, as they focused on the effects of adding a steady background flow to the slab in an asymmetric slab system. A different type of extension is
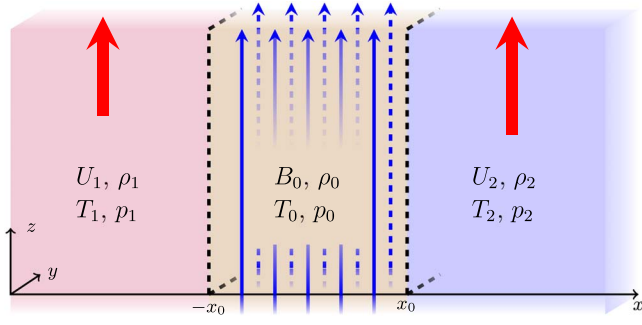
Figure 1. Equilibrium configuration of the slab. Red arrows indicate the external flows, while blue arrows show the internal magnetic field.

provided by Zaqarashvili et al. (2021), who analyzed the stability of solar jets in slab geometries subject to a kink oscillation. This last example ties into another important line of investigation when it comes to generalizing slab models, especially the ones under the effect of background flows, namely, that of introducing nonuniformity in some parameters. For example, a single interface was expanded into a transitional region by Tirry et al. (1998), who used the cold plasma approximation to study the threshold for the onset of the KHI, negative-energy waves, and resonant absorption in this nonuniform system. The effects of different velocity profiles on the KHI threshold have been investigated in slab-like layers and cylindrical geometries as well (see, e.g., Michalke 1964; Blumen 1970; Ray 1982; Wu & Wang 1991).

The problem of instabilities in a slab or flux tube mode, as illustrated above, can be approached from various directions, depending on which consequence of the presence of flows is to be studied. With the current work, our focus is on one specific aspect of the problem, namely, the consequence of flow asymmetries. To facilitate the understanding of this step of expanding slab system descriptions, we return to the type of piecewise uniform model generalized for kinetic asymmetry by Allcock & Erdélyi (2017) and for magnetic asymmetry by Zsámberger et al. (2018). Therefore, here we study MHD waves in an asymmetric slab configuration with no external magnetic fields, but with asymmetric background flows added to the external regions. Such a configuration may serve as a model of waves in, e.g., magnetic bright points (MBPs) in the solar photosphere, as they often show an elongated shape and can therefore be approximated by the model of an asymmetric slab to account for the different densities on their sides in the granular cells, or prominences sitting between two different regions of the solar corona. The model may also be applicable to spicule formation in the lower solar atmosphere, just at or above the photosphere.

2. The Dispersion Relation

We introduce a slab of plasma bounded by two interfaces at $\pm x_0$ of density ρ_0, pressure p_0, temperature T_0, and magnetic field $\boldsymbol{B}_0 = (0, 0, B_0)$. The slab is embedded in an asymmetric environment, defined as having density, pressure, and temperature ρ_1, p_1, and T_1 on the left side and ρ_2, p_2, and T_2 on the right side, which are subject to steady flows, $\boldsymbol{U}_1 = (0, 0, U_1)$ on the left and $\boldsymbol{U}_2 = (0, 0, U_2)$ on the right, as illustrated in Figure 1. The exterior is not subject to magnetic fields.

The governing equation for the disturbance within the magnetic slab can be obtained from the ideal MHD equations:

$$\rho \frac{d\boldsymbol{v}}{dt} = -\nabla p - \frac{1}{\mu_0} \boldsymbol{B} \times (\nabla \times \boldsymbol{B}), \tag{1}$$

$$\frac{\partial \rho}{\partial t} + \nabla \cdot (\rho \boldsymbol{v}) = 0, \tag{2}$$

$$\frac{d}{dt}\left(\frac{p}{\rho^\gamma}\right) = 0, \tag{3}$$

$$\frac{\partial \boldsymbol{B}}{\partial t} = \nabla \times (\boldsymbol{v} \times \boldsymbol{B}), \tag{4}$$

where the variables $\boldsymbol{v} = (v_x, v_y, v_z)$, $\boldsymbol{B}$, p, and ρ are the velocity, magnetic field, pressure, and density, respectively, at time t, and $d/dt = \partial/\partial t + (\boldsymbol{v}\nabla)$.

Since we are only concerned with magnetoacoustic waves propagating along the slab, parallel to the background magnetic fields we restrict ourselves to the choice of $k_y = 0$ and make the choice of $v_y = 0$, refraining from the study of, e.g., y-dependent Alfvén waves. In addition to purely magnetosonic waves propagating along the slab, a future extension of this study to $k_y \neq 0$ (i.e., nonparallel propagation to the magnetic field but still parallel with respect to the magnetic isosurfaces) can allow for the description of waves with mixed properties and further physical effects that influence the stability of the slab system. For example, Andries et al. (2000) studied the environment of coronal plumes including a nonuniform transitional layer in a slab and a flux tube model while allowing for the $k_y \neq 0$ case. They found that the resonant flow instability can occur at a lower velocity threshold than the KHI, which is a phenomenon that the current model cannot reproduce owing to the chosen restrictions and focus. After linearizing about a static basic state, we Fourier-decompose the equations to seek plane wave solutions propagating along the slab by assuming that $f(\boldsymbol{r}, t) = \hat{f}(x)e^{i(kz-\omega t)}$, where f stands for any of the small perturbations (pressure, density, velocity, and magnetic field) and $\hat{f}$ is the amplitude of each perturbation. Here ω is the angular frequency and k is the wavenumber in the z-direction. We can combine these equations to give an ordinary differential equation for, e.g., $\widehat{v_x}$, namely,

$$\widehat{v_x''} - m_0^2 \widehat{v_x} = 0, \tag{5}$$

where

$$m_0^2 = \frac{(k^2 v_A^2 - \omega^2)(k^2 c_0^2 - \omega^2)}{(c_0^2 + v_A^2)(k^2 c_T^2 - \omega^2)}, \quad c_T^2 = \frac{c_0^2 v_A^2}{c_0^2 + v_A^2}. \tag{6}$$

Here $c_j^2 = \gamma p_j/\rho_j$ ($j = 0, 1, 2$) is the sound speed, and $v_A^2 = B_0 / \sqrt{\rho_0 \mu}$ denotes the Alfvén speed of a given region. This expression describes the inside of the slab, and it is identical to the corresponding equation for a symmetric slab derived by Roberts (1981b). The same method may be applied to the exterior layers, with the consideration that in both semifinite regions there are no magnetic fields, but there are flows present. Therefore, the form of the m_j coefficients (for $j = 1, 2$) will be slightly different:

$$m_j^2 = k^2 - \frac{\Omega_j^2}{c_j^2}. \tag{7}$$

Here the exterior sound speeds are defined as $c_j^2 = \gamma p_j / \rho_j$ and $\Omega_j = \omega - kU_j$ for $j = 1, 2$ is the Doppler-shifted frequency.

We aim to find trapped wave modes that are evanescent outside the slab (i.e., all perturbations must vanish at $\pm\infty$), meaning that $m_j^2 > 0$ is required for $j = 1, 2$. This gives us the general solution of Equation (5) as

$$\widehat{v}_{xj}(x) = \begin{cases} A(\cosh(m_1 x) + \sinh(m_1 x)), & x < -x_0 \\ B\cosh(m_0 x) + C\sinh(m_0 x), & |x| \leqslant x_0 \\ D(\cosh(m_2 x) - \sinh(m_2 x)), & x > x_0, \end{cases} \quad (8)$$

where A, B, C, and D are arbitrary constants. By inspection, we establish that two wave modes are allowed to propagate under the given constraints: one that is evanescent toward the center of the slab (for $m_0^2 > 0$), and one that is spatially oscillatory throughout the slab (for $m_0^2 < 0$). These modes of propagation are the so-called surface and body modes, respectively (see, e.g., Roberts 1981b).

Equation (8) is subject to boundary conditions at the interfaces, namely, the continuity of the Lagrangian displacement and the continuity of total pressure:

$$\frac{\widehat{v}_{x1}(x = -x_0)}{\Omega_1} = \frac{\widehat{v}_{x0}(x = -x_0)}{\omega},$$
$$\frac{\widehat{v}_{x2}(x = x_0)}{\Omega_2} = \frac{\widehat{v}_{x0}(x = x_0)}{\omega},$$
$$[p_T]_{-x_0} = 0, \quad [p_T]_{x_0} = 0. \quad (9)$$

By substituting Equation (8) into the boundary conditions (9), we obtain a system of four coupled homogeneous algebraic equations:

$$\begin{pmatrix} (C_1 - S_1)/\Omega_1 & -C_0/\omega & S_0/\omega & 0 \\ 0 & -C_0/\omega & -S_0/\omega & (C_2 - S_2)/\Omega_2 \\ \Lambda_1(C_1 S_1) & \Lambda_0 S_0 & -\Lambda_0 C_0 & 0 \\ 0 & \Lambda_0 S_0 & \Lambda_0 C_0 & \Lambda_2(C_2 - S_2) \end{pmatrix}$$
$$\times \begin{pmatrix} A \\ B \\ C \\ D \end{pmatrix} = \begin{pmatrix} 0 \\ 0 \\ 0 \\ 0 \end{pmatrix}, \quad (10)$$

where, for brevity, we introduce $C_j = \cosh(m_j x_0)$, $S_j = \sinh(m_j x_0)$ for $j = 0, 1, 2$, and

$$\Lambda_0 = \frac{-i\rho_0(k^2 v_A^2 - \omega^2)}{m_0 \omega}, \quad \Lambda_1 = \frac{i\rho_1 \Omega_1}{m_1}, \quad \Lambda_2 = \frac{i\rho_2 \Omega_2}{m_2}. \quad (11)$$

For Equation (10) to have nontrivial solutions, we require the determinant of the matrix on the left-hand side to be equal to zero. Evaluating this condition, we obtain

$$2(\Lambda_0^2 \omega^2 + \Lambda_1 \Lambda_2 \Omega_1 \Omega_2) + \Lambda_0 \omega(\Lambda_1 \Omega_1 + \Lambda_2 \Omega_2)$$
$$\times (\tanh(m_0 x_0) + \coth(m_0 x_0)) = 0. \quad (12)$$

Using the notation introduced by Equation (11), we arrive at

$$m_0^2 \Omega_1^2 \Omega_2^2 + \frac{\rho_0}{\rho_1} m_1 \frac{\rho_0}{\rho_2} m_2 (k^2 v_A^2 - \omega^2)^2$$
$$- \frac{1}{2} m_0 (k^2 v_A^2 - \omega^2)\left(\frac{\rho_0}{\rho_1} m_1 \Omega_2^2 + \frac{\rho_0}{\rho_2} m_2 \Omega_1^2 \right)$$
$$\times (\tanh(m_0 x_0) + \coth(m_0 x_0)) = 0. \quad (13)$$

This is the general dispersion relation describing waves propagating along the magnetic field in a slab embedded in an asymmetric environment, in the presence of an asymmetric flow field. Similarly to the cases of the asymmetric slab system with (Barbulescu & Erdélyi 2018) or without (Allcock & Erdélyi 2017) an internal flow in a nonmagnetic environment, as well as to that of the slab in an asymmetric magnetic environment (Zsámberger et al. 2018), the dispersion relation is a single equation describing both main types of eigenmodes, which are called quasi-kink and quasi-sausage modes, following the naming convention established in Allcock & Erdélyi (2017).

The fact that the general dispersion relation cannot be decoupled into two separate equations for "traditional" sausage and kink eigenmodes is a mathematical consequence of the background asymmetry present in the slab system, which makes it so that the waves propagating in the slab interact with somewhat different environments on its two boundaries. This leads to changes in the well-known characteristics of sausage and kink modes in a symmetric slab system. A more detailed exploration of these changes and their dependence on the magnitude of the external asymmetry was provided, e.g., by Allcock & Erdélyi (2017), Zsámberger et al. (2018), Allcock & Erdélyi (2018), and Allcock et al. (2019).

The main differences between symmetric and asymmetric eigenmodes can be summarized as follows. For both types of solutions, the unsigned amplitudes of perturbations in the transverse velocity ($\widehat{v}_{xi}$, for $i = 0, 1, 2$) will be the same at the two boundaries of a symmetric slab, while in general they will be different in the asymmetric slab systems similar to the current model studied so far (see, e.g., Allcock & Erdélyi 2017; Barbulescu & Erdélyi 2018; Zsámberger et al. 2018). Furthermore, sausage modes in a symmetric slab show an unperturbed magnetic surface at the center of the slab. However, depending on the density and magnetic asymmetries, in an asymmetric slab system, this surface with zero perturbation is shifted toward one or the other slab boundary. Therefore, the central axis of the slab is not left unperturbed by quasi-sausage modes. In addition, asymmetric kink modes will be different from their symmetric counterparts too. Kink waves in a symmetric slab leave the slab's cross-sectional width unchanged, while quasi-kink modes in an asymmetric slab can generally change it. The lack of the purely sausage or purely kink character of oscillations raises new challenges in the identification of observed waves in an asymmetric system, which, e.g., Allcock & Erdélyi (2017) and Allcock et al. (2019) illustrate.

This constitutes a fundamental difference from symmetric slabs, which we look at in more detail in the next section.

2.1. Comparison with a Symmetric Slab

There is an intrinsic difference between perturbations along symmetric and asymmetric magnetic slabs. The dispersion relation governing an asymmetric slab is a single equation, describing waves of a mixed character, whereas the dispersion relation governing a symmetric slab (Roberts 1981b) consists of two

independent equations, corresponding to the sausage and kink eigenmodes.

A closer comparison to symmetric slab systems can be made if we require that the densities, pressures, and flow speeds on the two sides of the asymmetric slab should be of the same order, so that $\lambda_2 = \Lambda_2\Omega_2$ is of the same order as $\lambda_1 = \Lambda_1\Omega_1$. Then, $\lambda_2 = \lambda_1 + \epsilon$, and the following connection between these quantities may be made:

$$1 = \frac{1}{4}\frac{(\Lambda_1\Omega_1 + \Lambda_2\Omega_2)^2}{\Lambda_1\Omega_1\Lambda_2\Omega_2} + \mathcal{O}(\epsilon^2) \approx \frac{1}{4}\frac{(\Lambda_1\Omega_1 + \Lambda_2\Omega_2)^2}{\Lambda_1\Omega_1\Lambda_2\Omega_2}. \tag{14}$$

Substituting this into Equation (12), the full dispersion relation, multiplying by $2\Lambda_1\Omega_1\Lambda_2\Omega_2$ (which is a nonzero quantity) and factorizing, then yields

$$[\Lambda_0\omega(\Lambda_1\Omega_1 + \Lambda_2\Omega_2) + 2\Lambda_1\Omega_1\Lambda_2\Omega_2\tau_0]$$
$$\times \left[\Lambda_0\omega(\Lambda_1\Omega_1 + \Lambda_2\Omega_2) + 2\Lambda_1\Omega_1\Lambda_2\Omega_2\frac{1}{\tau_0} \right] = 0. \tag{15}$$

Setting either factor of this product as zero leads to an approximate dispersion relation for sausage- and kink-type modes separately under this so-called weak asymmetry approximation, which can be summarized as

$$\Lambda_0\omega(\Lambda_1\Omega_1 + \Lambda_2\Omega_2) + 2\Lambda_1\Lambda_2\Omega_1\Omega_2\binom{\tanh}{\coth}(x_0m_0) = 0. \tag{16}$$

The expressions for the variables Λ_i for $i = 0, 1, 2$ in Equations (11) can be substituted into this decoupled dispersion relation in order to express it in terms of the

$$\omega^2 = k^2c_T^2$$
$$\left[1 - \frac{2kx_0(c_0^2 - c_T^2)(c_T - U_1)^2(c_T - U_2)^2}{c_0^2 v_A^2\left[\frac{\rho_0}{\rho_1 c_1}(c_1^2 - (c_T - U_1)^2)^{1/2}(c_T - U_2)^2 + \frac{\rho_0}{\rho_2 c_2}(c_2^2 - (c_T - U_2)^2)^{1/2}(c_T - U_1)^2 \right]} \right], \tag{20}$$

characteristic speeds, densities, and wavenumber coefficients. After some rearranging, this leads to the following equation:

$$(k^2v_A^2 - \omega^2)\left(\frac{\rho_0}{\rho_1}m_1\Omega_2^2 + \frac{\rho_0}{\rho_2}m_2\Omega_1^2 \right)$$
$$= 2m_0\Omega_1^2\Omega_2^2\binom{\tanh}{\coth}(m_0x_0). \tag{17}$$

This is the decoupled dispersion relation for waves propagating in a weakly asymmetric magnetic slab system containing asymmetric background flows, expressed in terms of the characteristic speeds and densities of each region. Equation (17) is now in an analogous form to the dispersion relation corresponding to MHD waves along a symmetric magnetic slab (Roberts 1981b), namely,

$$(k^2v_A^2 - \omega^2)\frac{\rho_0}{\rho_e}m_e = \omega^2m_0\binom{\tanh}{\coth}(m_0x_0), \tag{18}$$

where external parameters are denoted by subscript e. Indeed, if the differences in external densities and flow speeds are

reduced to zero, the symmetric dispersion relation may be recovered from Equation (17).

3. Analytical Solutions

In this section, simplifications are made to the dispersion relation, Equation (13), and approximate dispersion relation, Equation (17), in order to provide tractable analytical solutions. First, the simplifications by fixing the slab width are examined, and then approximate solutions based on fixing the plasma-β in the three regions are presented.

3.1. The Effects of the Slab Width

3.1.1. Thin-slab Approximation

Consider the case where the wavelength of waves propagating in the system is much greater than the width of the slab, $2x_0$, and therefore $kx_0 \ll 1$.

Surface waves: Let us investigate surface waves, which are characterized by $m_0^2 > 0$. First, consider the quasi-sausage surface mode, which is governed by the tanh version of Equation (17), for $m_0^2 > 0$. In the thin-slab limit, this equation reduces to

$$(k^2v_A^2 - \omega^2)\left(\frac{\rho_0}{\rho_1}m_1\Omega_2^2 + \frac{\rho_0}{\rho_2}m_2\Omega_1^2 \right) = 2m_0\Omega_1^2\Omega_2^2m_0x_0. \tag{19}$$

There is a solution for this equation where ω^2 behaves like $\omega^2 \to k^2c_T^2$ as $kx_0 \to 0$. To first order in kx_0, this solution describing a slow sausage surface mode is given by

which is less than $k^2c_T^2$ and exists only when $c_1 > c_T - U_1$ and $c_2 > c_T - U_2$.

Next, consider quasi-kink surface mode solutions in the thin-slab limit, which are governed by the coth version of Equation (17), for $m_0^2 > 0$. As $kx_0 \to 0$, we have $m_0x_0 \to 0$, so $\coth(m_0x_0) \to 1/m_0x_0$. This leads to another solution of the dispersion relation, which describes a quasi-kink surface mode:

$$\omega^2 = k^2v_A^2 - \frac{2kU_1^2U_2^2}{x_0\left(\frac{\rho_0}{\rho_1}\frac{(c_1^2 - U_1^2)^{1/2}}{c_1}U_2^2 + \frac{\rho_0}{\rho_2}\frac{(c_2^2 - U_2^2)^{1/2}}{c_2}U_1^2 \right)}. \tag{21}$$

Body waves: For body waves, $m_0^2 < 0$, and solutions are spatially oscillatory inside the slab. In order to highlight the relation between the angular frequencies of body modes and the flow speeds, it is possible to change the coordinate system into one moving with the flow speed on one side of the slab, say, U_1. Then, the new flow speeds are defined as $U_{1,\text{new}} = 0$, $U_{0,\text{new}} = -U_1$, and $U_{2,\text{new}} = U_2 - U_1$, leading to the following new form of the angular frequencies: $\Omega_{1,\text{new}} = \omega$, $\Omega_{0,\text{new}} = \omega - kU_{0,\text{new}}$, and $\Omega_{2,\text{new}} = \omega - U_{2,\text{new}}$. With these

definitions, the decoupled dispersion relation for body waves becomes

$$N_0^2 = -M_0^2 = -\frac{(k^2 v_A^2 - \Omega_{0,\text{new}}^2)(k^2 c_0^2 - \Omega_{0,\text{new}}^2)}{(c_0^2 + v_A^2)(k^2 c_T^2 - \Omega_{0,\text{new}}^2)},$$

$$m_1 = \left(\frac{k^2 c_1^2 - \omega^2}{c_1^2}\right)^{1/2},$$

$$M_2 = \left(\frac{k^2 c_i^2 - \Omega_{2,\text{new}}^2}{c_i^2}\right)^{1/2}. \tag{22}$$

For quasi-sausage body modes, in order for the $N_0 \tan(N_0 x_0)$ term in the dispersion relations to remain finite as $k x_0 \to 0$, it is required that $N_0 x_0$ tend to the roots of $\tan(N_0 x_0) = 0$, so $N_0 x_0 \to j\pi$ for integer values of j. Slow body mode solutions can be described as $\Omega_{0,\text{new}}^2 = k^2 c_T^2 (1 + \nu(k x_0)^2)$. By substituting this form of $\Omega_{0,\text{new}}$ into the abovementioned condition on $N_0 x_0$, an approximate analytical description of the slow body quasi-sausage modes can be obtained. Quasi-kink mode solutions can be approximated in a similar manner, only, in their case, $N_0 x_0$ must tend to the roots of $\cot(N_0 x_0) = 0$, so $N_0 x_0 \to (j - 1/2)\pi$. Using the conditions described here, the slow quasi-sausage and quasi-kink body modes can be described as

$$\omega = k U_{0,\text{new}} \pm k c_T \sqrt{1 + \frac{c_T^4 (k x_0)^2}{c_0^2 v_A^2 \pi^2 q^2}}, \tag{23}$$

where $q = j$ for quasi-sausage modes and $q = j - 1/2$ for quasi-kink modes ($j = 1, 2, \ldots$). Equation (23) shows us that to quadratic order in $k x_0$, the quasi-sausage and quasi-kink body modes do not depend on the external environmental parameters (as in Allcock & Erdélyi 2017).

3.1.2. Wide-slab Approximation

As opposed to the previous case, it is also possible that the wavelength of propagating waves is much shorter than the width of the slab, and so $k x_0 \gg 1$. In the wide-slab approximation, both $\tanh(n_0 x_0)$ and $\coth(n_0 x_0)$ in Equation (17) have large arguments and become approximately one. Therefore, the approximate dispersion relation for surface waves in a wide slab is

$$(k^2 v_A^2 - \omega^2)\left(\frac{\rho_0}{\rho_1} M_1 \Omega_2^2 + \frac{\rho_0}{\rho_2} M_2 \Omega_1^2\right) = 2 m_0 \Omega_1^2 \Omega_2^2. \tag{24}$$

Similarly to the behavior described in Allcock & Erdélyi (2017) and Zsámberger & Erdélyi (2020), quasi-sausage and quasi-kink surface waves in a wide asymmetric slab system including external flows tend to different phase speed limits, which depend on the magnitude of the external asymmetry. Slow and fast body modes in a wide slab can be described together. It depends on the ordering of the internal and external characteristic speeds whether they can be present and, if they are, which value their phase speed approaches. Using the shifted coordinate system from before and defining $v_{\text{max}} = \max(v_A, c_0)$ and $v_{\text{min}} = \min(v_A, c_0)$, slow body waves can be described as $\Omega_{0,\text{new}}^2 = k^2 v_{\text{min}}^2 (1 - \nu/(k x_0)^2)$. By a reasoning similar to the case of the thin slab, in the case of quasi-sausage modes, for the $N_0 \tan(N_0 x_0)$ term to remain nonzero and finite, $N_0 x_0 = (j - 1/2)\pi$ ($j = 1, 2, \ldots$) is required. For quasi-kink modes,

$N_0 x_0 = j\pi$, so that $N_0 \cot(N_0 x_0)$ will remain finite and nonzero. Combining these requirements, slow body modes in a wide slab can be described as

$$\omega = k U_{0,\text{new}} \pm k v_{\text{min}}\left(1 - \frac{q^2 \pi^2 v_{\text{min}}^2}{[v_{\text{max}}^2 - v_{\text{min}}^2][k x_0]^2}\right)^{1/2}, \tag{25}$$

where $q = j - 1/2$ for quasi-sausage modes and $q = j$ for quasi-kink modes. Following the same notation and arguments, fast body modes, if they exist, can be approximated in a wide slab as

$$\omega = k U_{0,\text{new}} \pm k v_{\text{max}}\left(1 - \frac{q^2 \pi^2 v_{\text{max}}^2}{[v_{\text{max}}^2 - v_{\text{min}}^2][k x_0]^2}\right)^{1/2}. \tag{26}$$

3.2. The Effects of the Choice of Plasma-β

The plasma-β parameter is a simple way to characterize and measure the relative magnitude of magnetic and pressure gradient forces, defined as $\beta = p_{\text{mag}}/p = (2/\gamma) v_A^2 / c_s^2$. The effect of various choices of plasma-β throughout the asymmetric magnetic slab system without flows has been investigated in Zsámberger & Erdélyi (2020). Here we provide several useful analytical approximations of the dispersion relation and its solutions for different practical ranges of the plasma-β parameter popular in solar physics applications in the absence of external magnetic fields, but in the presence of asymmetric external flows.

3.2.1. High-β Approximation

Generally, a slab system in which all three regions have a high plasma-β can be a good approximation of a photospheric environment in the solar atmosphere or in subsurface regions. In the simplest and analytically most tractable case of the $\beta \to \infty$ approximation, the Alfvén speed is negligible compared to the sound speed ($v_A \to 0$). Then, the coefficients related to wavenumbers become

$$n_0^2 = -m_0^2 = -\frac{k^2 c_0^2 - \omega^2}{c_0^2} \qquad \text{for } i = 0, \text{ and}$$

$$M_i^2 = \frac{k^2 c_i^2 - \Omega_i^2}{c_i^2} \qquad \text{for } i = 1, 2. \tag{27}$$

In the high-β slab placed in an asymmetric environment, fast body modes exist, which are described by the following dispersion relation:

$$\left(\begin{array}{c}\tan \\ -\cot\end{array}\right)(n_0 x_0) = -\frac{1}{2}\left(\frac{\rho_0}{\rho_1}\frac{M_1}{n_0}\frac{\omega^2}{\Omega_1^2} + \frac{\rho_0}{\rho_2}\frac{M_2}{n_0}\frac{\omega^2}{\Omega_2^2}\right). \tag{28}$$

Setting the flow speeds to zero and eliminating the external asymmetry reduces this equation to the expression valid in the symmetric case, described in Equations (24) and (25) in Edwin & Roberts (1982).

3.2.2. Low-β Approximation

If the plasma-β inside the slab is very low, then the internal sound speed becomes negligible compared to the Alfvén speed. In the simplest case of the zero-β approximation, the

wavenumbers become

$$n_0^2 = -m_0 = -\frac{k^2 v_A^2 - \omega^2}{v_A^2} \qquad \text{for } i = 0, \text{ and}$$

$$M_i^2 = \frac{k^2 c_i^2 - \Omega_i^2}{c_i^2} \qquad \text{for } i = 1, 2. \qquad (29)$$

In the zero-β slab placed in an asymmetric, nonmagnetic environment, fast body modes can exist, described by the following dispersion relation:

$$\begin{pmatrix} \tan \\ -\cot \end{pmatrix} (n_0 x_0) = \frac{1}{2} \frac{\sqrt{k^2 v_A^2 - \omega^2}}{v_A} \left(\frac{\rho_0}{\rho_1} \frac{M_1}{\Omega_1^2} + \frac{\rho_0}{\rho_2} \frac{M_2}{\Omega_2^2} \right). \quad (30)$$

3.3. Dependence on Density and Flow Asymmetry

3.3.1. Quasi-sausage Modes

In order to better understand how the degree of external density asymmetry, as well as the direction of and difference between the magnitudes of external flow speeds, affects which waves a weakly asymmetric magnetic slab supports, it is possible to provide expansions of the solutions to the dispersion relation in terms of two small parameters. Namely, these are the density asymmetry, defined as

$$\delta = \frac{\rho_2 - \rho_1}{\rho_1}, \qquad (31)$$

and the flow asymmetry,

$$\varepsilon = \frac{U_2 - U_1}{U_1}. \qquad (32)$$

Using these small parameters, we can expand the expressions for the slow surface wave solutions in the limit of a thin slab, in order to study the effect of different kinds of asymmetry on the phase speed of waves, as well as on the onset of the KHI. Keeping terms to first order in ϵ and δ, the angular frequency of the slow sausage surface mode in the thin-slab limit is then

$$\omega^2 = k^2 c_T^2 (1 - A_s[B_s + C_s \delta + D_s \epsilon]), \qquad (33)$$

where

$$A_s = \frac{\rho_1}{\rho_0} \frac{[c_0^2 - c_T^2][c_T - U_1] c_1 k x_0}{2\sqrt{c_1^2 - [c_t - U_1]^2} \, v_A^2 c_0^2}, \qquad (34)$$

$$B_s = 2\{c_T - U_1\}, \qquad (35)$$

$$C_s = \{c_T - U_1\} \left\{ 1 + \frac{(c_T - U_1)^2}{2(c_1^2 - [c_T - U_1]^2)} \right\}, \qquad (36)$$

$$D_s = \frac{(c_T - U_1)^2}{\{c_1^2 - (c_T - U_1)^2\}} U_1. \qquad (37)$$

From this solution, a limiting density parameter can be expressed, meaning that if the density asymmetry is larger than a certain value (given by the background parameters and the flow asymmetry), the KHI can appear in the slab system. This limit is given as

$$\epsilon > \frac{1}{D_s} \left(\frac{1}{A_s} - B_s - C_s \delta \right), \qquad (38)$$

if $A_s > 0$ and $D_s > 0$, which requires that $c_1^2 > (c_T - U_1)^2$ and $c_T > u_1$.

Alternately, for a given flow asymmetry, a critical density asymmetry value can also be found that takes ω^2 below zero and gives rise to the KHI:

$$\delta > \frac{1}{C_k} \left(\frac{1}{A_k} - B_k - D_k \epsilon \right), \qquad (39)$$

if $A_k > 0$ and $C_k > 0$, which means that $c_1^2 > (c_T - U_1)^2$, $c_T > u_1$, and $-2 < (c_T - U_1)^2/(c_1^2 - [c_T - U_1]^2)$.

3.3.2. Quasi-kink Modes

Similarly, for slow quasi-kink surface waves, the angular frequency depends on the density and flow asymmetries as

$$\omega^2 = k^2 v_A^2 (1 - A_k[B_k + C_k \delta + D_k \epsilon]), \qquad (40)$$

where

$$A_k = \frac{\rho_1}{\rho_0} \frac{2U_1^2 c_1}{4 v_A^2 [c_1^2 - U_1^2]^{3/2} k x_0}, \qquad (41)$$

$$B_k = 2\{c_1^2 - U_1^2\}, \qquad (42)$$

$$C_k = \left\{ U_1^2 + \frac{2(c_1^2 - U_1^2)^2}{2} - \frac{c_1^2}{2} \right\}, \qquad (43)$$

$$D_k = \{2(c_1^2 - U_1^2) - U_1^2\}. \qquad (44)$$

The KHI sets in when

$$\epsilon > \frac{1}{D_k} \left(\frac{1}{A_k} - B_k - C_k \delta \right), \qquad (45)$$

if $A_k > 0$ and $D_k > 0$, which requires that $2/3 c_1^2 > U_1^2$.

As before, a critical value of density asymmetry giving rise to the KHI can also be found:

$$\delta > \frac{1}{C_k} \left(\frac{1}{A_k} - B_k - D_k \epsilon \right), \qquad (46)$$

if $A_k > 0$ and $C_k > 0$, which means $c_1^2 > U_1^2$ and $3/2 c_1^4 + 1/2 U_1^4 > (3c_1^2 - 1/2) U_1^2$.

4. Numerical Results

We now proceed to find the general solutions to the dispersion relation, Equation (13). Since, to the best of our knowledge, these cannot be obtained analytically, we employ a numerical scheme. We first nondimensionalize all quantities with respect to the Alfvén speed and introduce the Alfvén Mach numbers $M_{Aj} = U_j/v_A$ $(j = 0, 1, 2)$, the dimensionless sound speeds $\bar{c}_j^2 = c_j^2/v_A^2$ $(j = 0, 1, 2)$, tube speed $\bar{c}_T^2 = c_T^2/v_A^2$, and phase speed $\bar{c}_{ph} = c_{ph}/v_A = \omega/k v_A$.

Dispersion diagrams displaying general solutions to Equation (13) may be found in Figure 2. These graphs immediately show that the asymmetric background flows have broken the symmetry between forward- and backward-propagation solutions in both cases, regardless of whether those flows point in opposite directions (Figure 2(a)) or in the same direction (Figure 2(b)). To generate these figures, we have chosen photospheric values for the parameters, say, $c_0 = 11$ km s^{-1} and $v_A = 12$ km s^{-1} (Keys et al. 2013), $c_1 = 8$ km s^{-1} and $c_2 = 7$ km s^{-1} (Hurlburt et al. 2002), and $v_{A1} = v_{A2} = 0$ km s^{-1} (Felipe et al. 2016; Jiang et al. 2011). Estimates for
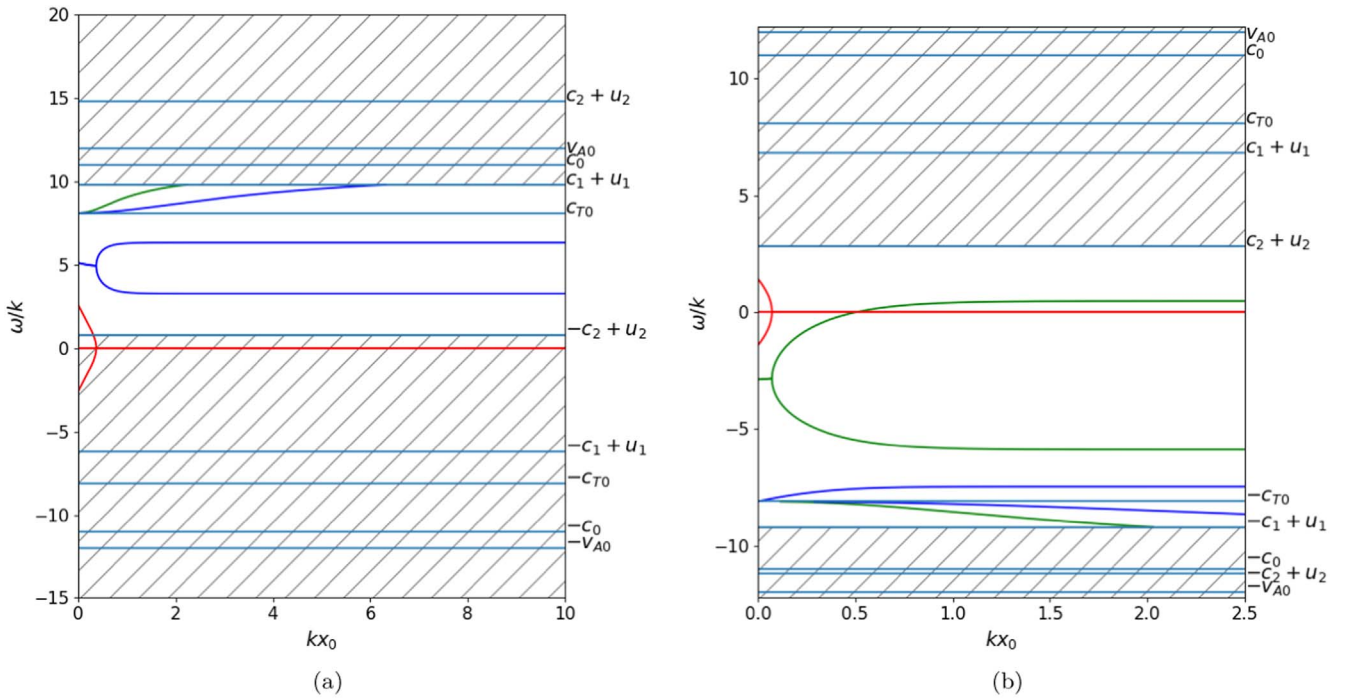
Figure 2. Dispersion diagrams, where green (blue) lines show the real part of the quasi-kink (quasi-sausage) mode phase speeds, and red lines display their imaginary parts. The slab and its environment have background flows of Alfvén Mach numbers (a) $M_{A0} = 0$, $M_{A1} = 0.15$, and $M_{A2} = 0.65$ and (b) $M_{A0} = 0$, $M_{A1} = -0.1$, and $M_{A2} = -0.35$. The hatched areas represent regions where there are no trapped solutions.

downflow speeds in the immediate surroundings of small magnetic elements range from as low as 1 km s^{-1} to even 10 km s^{-1} (Briand & Solanki 1998; Socas-Navarro et al. 2004; Danilovic et al. 2010). Choosing values within these ranges for our numerical investigation allows us to see how the different flows affect the phase speeds and stability of MHD waves present in the system.

Effects of upflows characterized by $M_{A0} = 0$, $M_{A1} = 0.15$, and $M_{A2} = 0.65$ are depicted in the left panel. Surface waves can be found between $-c_2 + U_2$ and c_{T0}, whereas body waves can be found between c_{T0} and $c_1 + U_1$ (for better visibility, we have only plotted two body waves as an example, out of the infinitely many harmonics possible). We also observe that, in the thin-slab limit, the surface waves are Kelvin–Helmholtz unstable, as seen by the growing imaginary part of the solutions (signified by the red curve).

Effects of downward flows with typical values of, e.g., $M_{A0} = 0$, $M_{A1} = -0.1$, and $M_{A2} = -0.35$ can be seen in the right panel. Surface waves can be found between $-c_{T0}$ and $c_2 + U_2$, whereas body waves can be found between $-c_1 + U_1$ and $-c_{T0}$. Although the figures look qualitatively different, as the new choice of flows has changed the phase speeds of the trapped oscillations a lot, it is still the thin slabs that are subject to the KHI, as before. This second figure could model the case of an MBP. MBPs are small concentrations of intense magnetic field in the photosphere, enclosed in between two segments of intergranular lane with similar characteristics to the ones presented above. They often display an elongated shape, which makes it possible to treat them as asymmetric magnetic slabs (for more details, see Zsámberger et al. 2018; Zsámberger & Erdélyi 2021).

Expanding the results for a certain choice of flow asymmetry and slab width depicted in Figure 3, as well as the similar series of figures in the supplementary material related to Figures 4 and 5, a number of interesting observations can be made about

the behavior of waves in the presence of asymmetric flows in the slab system.

If we start analyzing the diagram in Figure 3 from the origin, the first region of interest appears in the shape of a "central oval." In this region (for the given set of background parameters), a slow kink mode and sausage mode are both present and stable. The blue lines here show the real part of the phase speeds of these oscillations, while the red line, which remains at a constant value of zero for this region, depicts the imaginary part of the phase speeds. Additionally, at higher phase speed values in both the forward- and backward-propagating areas of the diagram, some body modes are also present. These are stable in this range of M_{A2}, and they even remain stable for higher and lower flow speeds on the right-hand side of the slab system.

It is noteworthy that this "central region" of stability is not centered at the origin, but it is shifted instead—in this case, toward negative Alfvén Mach number and phase speed values. As will be shown later, the shift depends on the choice of flow speeds and their asymmetry.

Outside this first region, for relatively small positive M_{A2} values, the surface waves become Kelvin–Helmholtz unstable, and the imaginary part of the phase speeds grows rapidly, as shown by the red lines in Figure 5. The increasing flow speed in the right-hand region of the slab's environment also affects the phase speeds of the supported modes, which leads to the body modes with negative phase speeds becoming leaky in this region.

On the negative (i.e., counter bulk motion) side of the M_{A2} axis, we find ever-larger external downflows, which leads to similar effects. Once $|M_{A2}|$ is larger than the threshold value, the surface modes become subject to the KHI. Additionally, the backward-propagating body modes are present and stable in the whole domain of negative M_{A2} values, while the forward-propagating ones already become leaky for relatively small downflows.
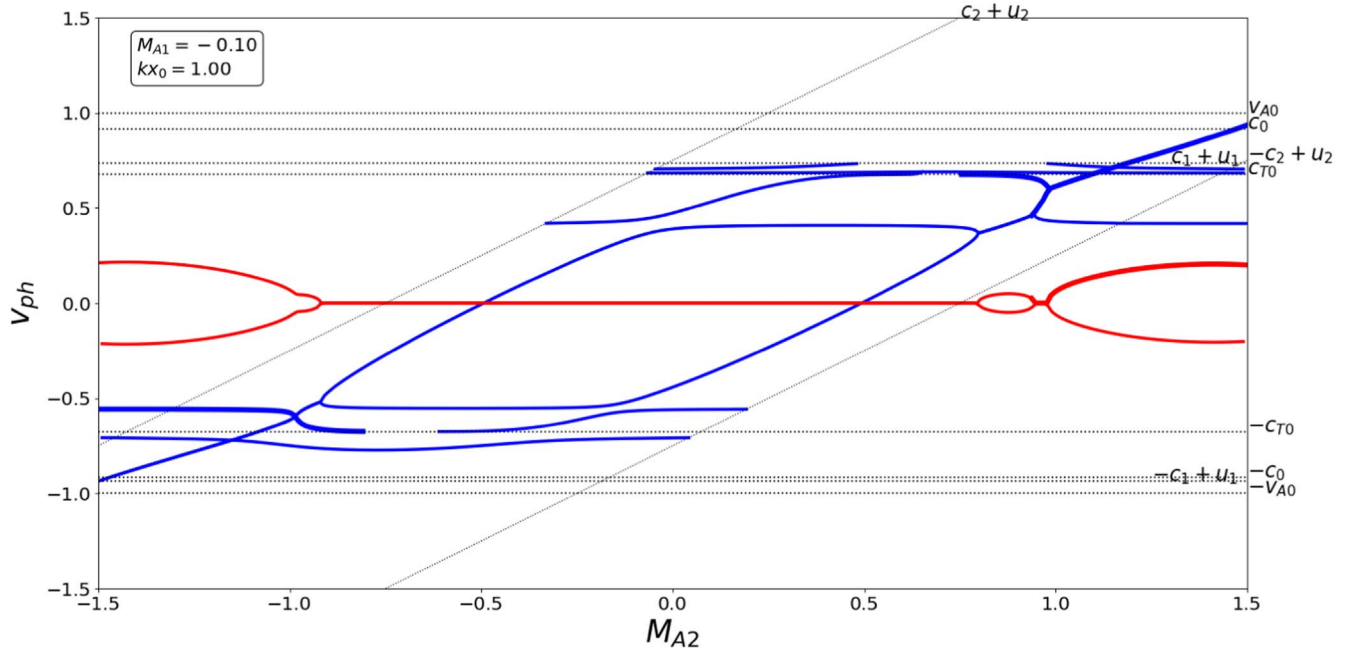
Figure 3. Changes in the phase speed of trapped oscillations in a slab of intermediate width ($kx_0 = 1$) caused by changing the flow speed on one side of the slab ($M_{A2} = u_2/v_A$) while keeping the flow speed on the other side fixed. The real part of the phase speed values is displayed in blue, while the imaginary part is shown in red. The Alfvén Mach numbers used to obtain these solutions were $M_{A0} = 0$, $M_{A1} = -0.1$, while M_{A2} changed from -1.5 to 1.5, representing both up- and downflows on the right-hand side of the slab.
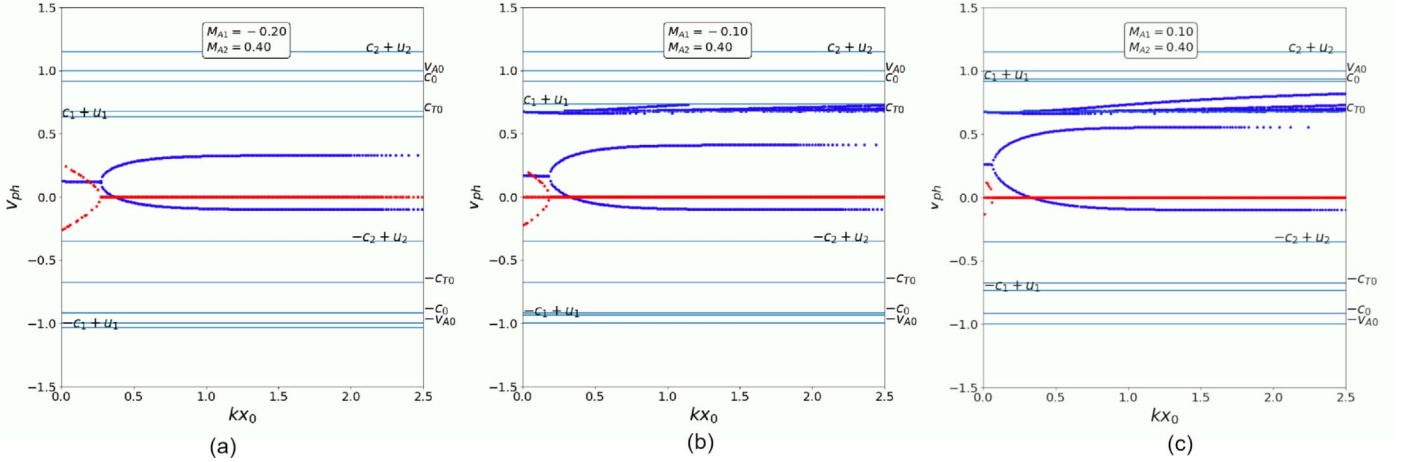

Figure 4. Dispersion diagrams of trapped oscillations in a magnetic slab, where the asymmetric environment has a fixed flow to the left and a gradually changing flow to the right of the slab. The real (imaginary) parts of the solutions are plotted in blue (red). In panel (a) the speed of the left-hand-side flow is $M_{A1} = -0.2$, while in panel (b) it is $M_{A1} = -0.1$ and in panel (c) it is $M_{A1} = 0.1$. All diagrams were prepared using the background parameters $v_{A0} = 12$ km s^{-1}, $c_0 = 11$ km s^{-1}, $c_1 = 8$ km s^{-1}, $c_2 = 7$ km s^{-1}, normalized by the internal Alfvén speed, and $\rho_1/\rho_0 = 2.41$, $\rho_2/\rho_0 = 2.98$. An interactive version of each figure is available, in which the Alfvén Mach number on the right-hand side of the slab is changing between frames from $M_{A2} = -1.5$ to $M_{A2} = 1.5$ by steps of 0.1, while every other background parameter remains the same, illustrating how increasing or decreasing the flow asymmetry leads to the presence of different trapped, stable and unstable solutions.
(An animation of this figure is available.)

There are two fundamental parameter changes that call for further examination. First, the selection of which eigenmodes are stable is also affected by the width of the slab. This can easily be seen from Figure 2, which depicts trapped solutions as a function of the nondimensional slab width, for a fixed value of the external Alfvén Mach numbers. Figure 3, on the other hand, shows stable and unstable trapped oscillations for a slab of intermediate width ($kx_0 = 1$), as well as how these solutions depend on the magnitudes of the flows outside the slab. The supplementary animation of Figure 5

illustrates this effect further: as kx_0 is gradually increased, the "central region" of stability also grows in its extent, and ever-higher $|M_{A2}|$ values are required for the onset of instability.

The trend we can see from both these comparisons is that the narrower our slab is, the smaller the second external flow speed can be for the surface modes to become subject to the KHI. This connection between the slab width and the limiting flow speed for the onset of the KHI is also reflected in our approximate solution in Equation (40).
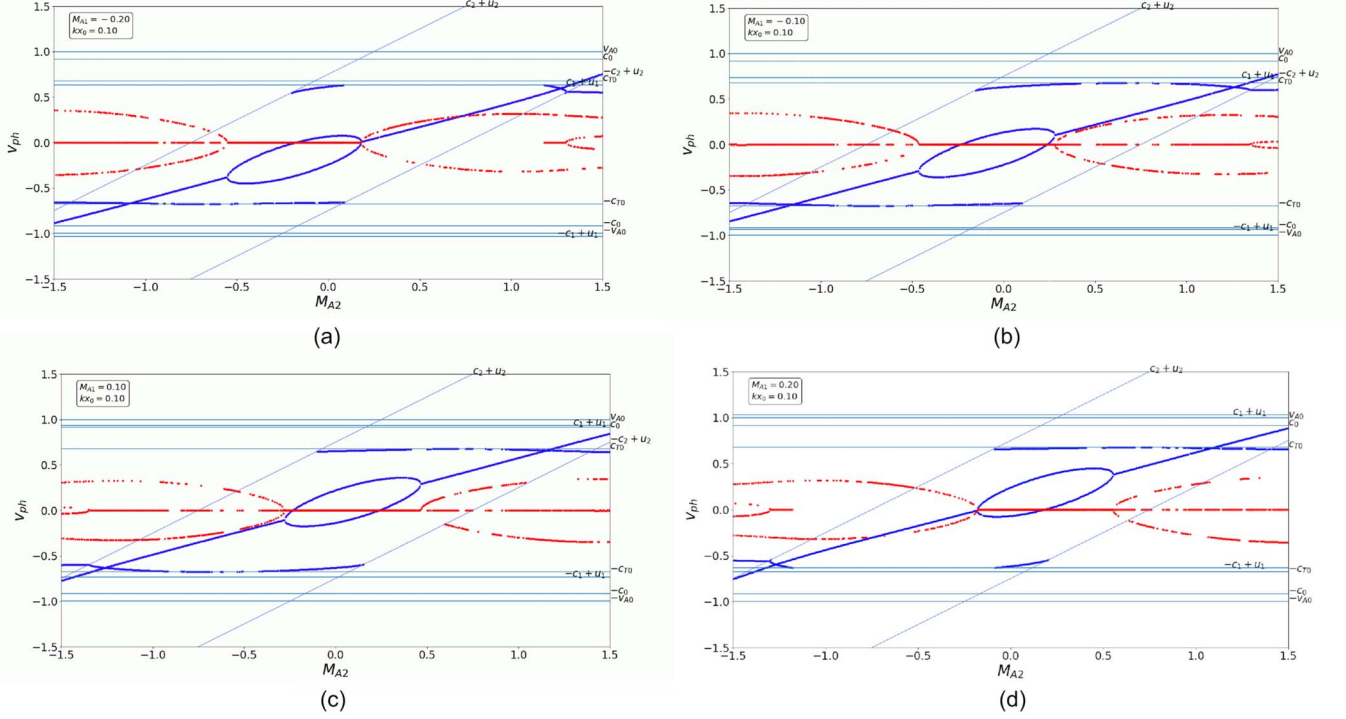
Figure 5. Phase speeds of trapped oscillations in a magnetic slab as a function of the external Alfvén Mach number on the right-hand side, for various slab widths, kx_0. As in Figure 4, the asymmetric environment has a fixed flow to the left of the slab. The real (imaginary) parts of the solutions are plotted in blue (red). In panel (a), the left-hand-side flow is $M_{A1} = -0.2$; in panel (b), it is $M_{A1} = -0.1$; in panel (c), it is $M_{A1} = 0.1$; and in panel (d), it is $M_{A1} = 0.2$. An animated version of all three figures is available, where the slab width changes in every frame, growing from $kx_0 = 0.05$ to $kx_0 = 0.95$ with a step size of 0.05, while all the background speeds and flows remain the same, showing how the relative sizes of the stable and unstable regimes of trapped waves change.

(An animation of this figure is available.)

The second important parameter is the magnitude and direction of the fixed flow on the left-hand side. All our analytical solutions show a definite dependence on this flow speed, and the expansions with respect to small parameters also reveal a connection with the flow asymmetry.

Our series of figures and videos in Figure 4 show the phase speeds of trapped oscillations as a function of the slab width at various values of M_{A2} and therefore flow asymmetry. In the animation of Figure 4, we have prepared a series of solutions for very small ($M_{A1} = -0.1$) and somewhat larger ($M_{A1} = -0.2$) downflows and a small upflow on one side ($M_{A1} = 0.1$). These series of solutions show that the KHI occurs more easily in thin slabs in general, and larger flow speeds are needed to make wider slabs KHI unstable too. This process is further amplified by a contribution from flow asymmetry: as the difference between the magnitude of the flows on the two sides of the slab grows, instability sets in for an ever-wider range of slab widths (wavelengths). Because by themselves the flows in our example are relatively weak (characterized by Alfvén Mach numbers between -0.2 and 0.1) when they are symmetric, the slab can even remain stable for all wavenumbers in such a situation.

As mentioned above, choosing a different fixed flow resulted in various trapped modes and instability limits for the solutions plotted in Figure 2. The series of solutions shown in Figure 4 and the supplementary material attached further illustrate the connection between phase speeds, instability limits, and the asymmetry present in the external background flows. A simple, visual way to qualitatively describe this effect is to say that the choice of flow speeds and asymmetry will essentially shift the position of the "central oval" of stability. This shift can be seen
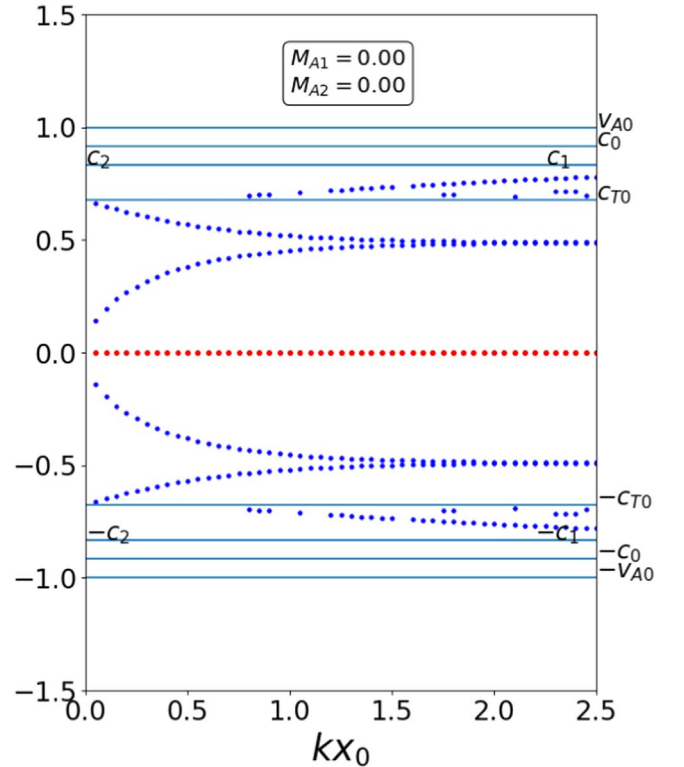

Figure 6. Phase speed of waves in a symmetric magnetic slab with no flows in any region, prepared using background parameter values of $c_0 = 11$ km s^{-1}, $v_A = 12$ km s^{-1}, $c_e = 8$ km s^{-1}, $\rho_e/\rho_0 = 2.41$. The real (imaginary) parts of the solutions are plotted in blue (red).
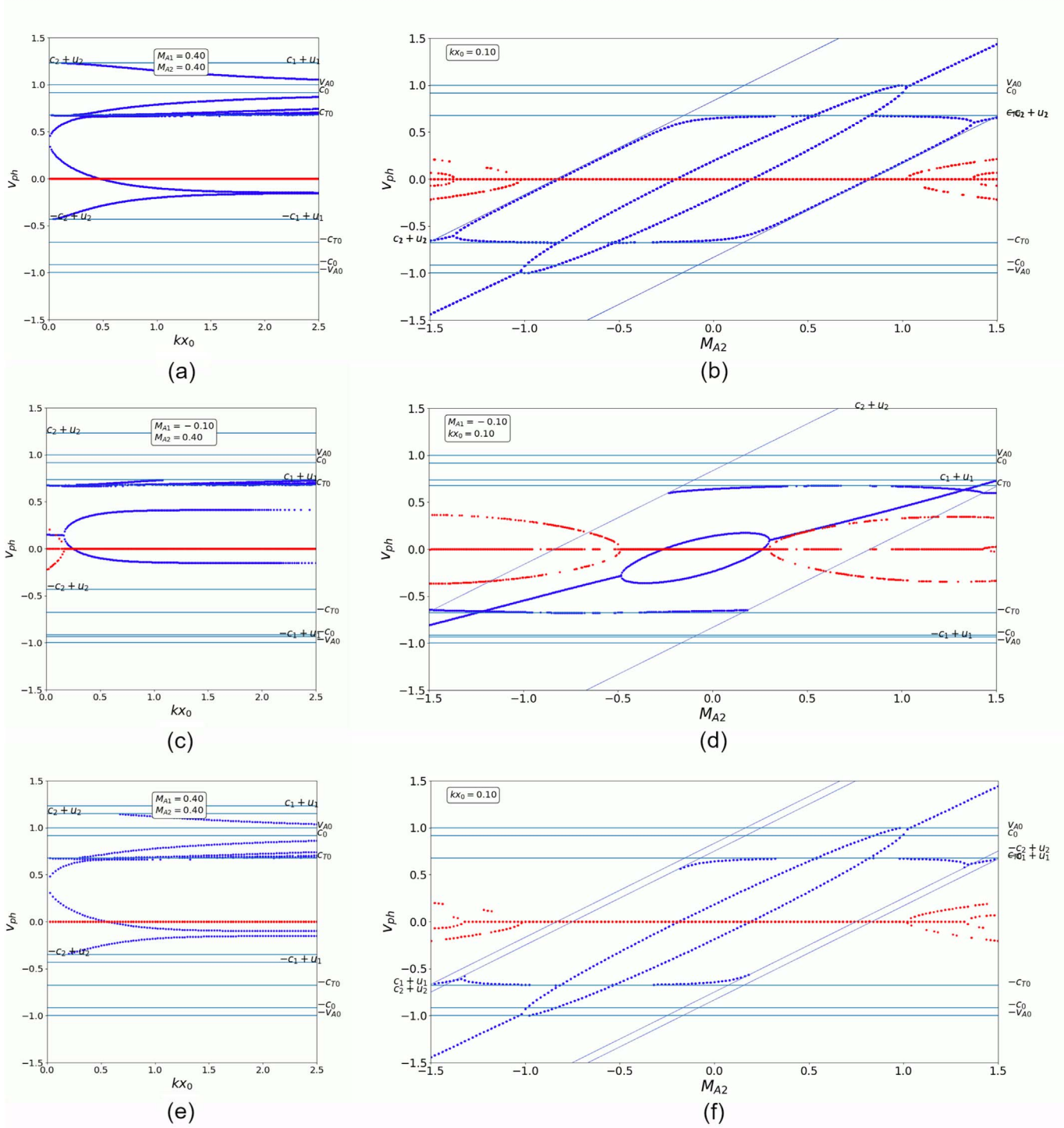
Figure 7. Phase speeds of trapped oscillations as a function of (a, c, e) slab width and (b, d, f) right-hand-side flow speed. Panels (a) and (b) display solutions for a magnetic slab embedded in a symmetric environment, where the environmental regions have symmetric flows. In order to preserve the flow symmetry, the left-hand-side Alfvén Mach number changes along with M_{A2} from left to right in panel (b). Panels (c) and (d) show solutions in a magnetic slab embedded in a symmetric environment, where the environmental regions have asymmetric flows. Panels (e) and (f) show the phase speeds of trapped oscillations in a magnetic slab embedded in an asymmetric environment. In panel (f), to preserve the flow symmetry, M_{A1} and M_{A2} change together, like in panel (a). The real (imaginary) parts of the solutions are plotted in blue (red). Animated versions of all six panels are available. The animations based on panels (a), (c), and (d) change the right-hand-side Alfvén Mach number between frames from $M_{A2} = -1.5$ to $M_{A2} = 1.5$ with a step size of 0.1. Animations based on panels (a) and (e) change M_{A1} along with M_{A2} in each step to keep the flow symmetry intact, while the animation based on panel (c) keeps M_{A1} fixed along with all other background parameters. They show how the possible modes and stability limits shift for various slab widths between systems subject to different external flows. Animations based on panels (b), (d), and (f) change the slab width frame by frame from $kx_0 = 0.05$ to $kx_0 = 0.95$ by steps of 0.05, while keeping all other background parameters intact. These animations illustrate how various systems subject to external flows of the same strength will support different trapped modes and have different stability limits depending on how wide the central slab is.

(An animation of this figure is available.)

by comparing the results for various fixed flows and slab widths in Figure 5.

Furthermore, it is interesting to trace how introducing various kinds of asymmetries into the model influences the phase speeds of trapped waves and the instability thresholds. In Figure 6, we plotted solutions for the case of a symmetric slab with no flows present, when $c_0 = 11$ km s^{-1}, $v_A = 12$ km s^{-1}, $c_e = c_1 = c_2 = 8$km s^{-1}, $\rho_e/\rho_0 = \rho_1/\rho_0 = \rho_2/\rho_0 = 2.41$, $M_{A0} = 0$, $M_{A1} = -0.1$, and $M_{A2} = -0.35$.

This is comparable to Roberts (1981b), where we have a (low-β) magnetic slab embedded between two regions of nonmagnetized plasma. In this figure, we kept the notation $c1$ and $c2$ for the sound speeds of the external regions for the sake of consistency, but in fact they are both equal (denoted as c_e in Roberts II), as are the external densities: $\rho_1 = \rho_2 = \rho_e$. In this case, there are no external asymmetries present to break the phase speed symmetry between backward- and forward-propagating modes: in both directions, a pair of slow surface waves and a band of body wave harmonics can be found as trapped modes.

In Figures 7(a) and (b), we implemented symmetric downflows $(M_{A1} = M_{A2} = M_{Ae})$ into the previous model. This resulted in a change of the phase speed limits posed by the external sound speeds ($c_i + u_i$, where $i = 1$, 2), as well as the phase speed of the previously identified trapped waves themselves. However, because of the symmetric flows, all of the modes found in the static case still existed, and the slab remained stable against the KHI. Such a steady slab system corresponds to the cases investigated by Nakariakov & Roberts (1995).

In Figures 7(a) and (b), we show the consequences of changing this symmetric flow speed. In general, trapped modes can still only exist between $-c_e + u_e$ and $c_e + u_e$. However, they get swept backward or forward by different amounts against a static background as the flow speeds keep changing. Between $M_{Ae} = -1$ and $M_{Ae} = 1$, the slab remains stable, but for higher flow magnitudes, various regions of instability appear, first in thinner slabs and then at all slab widths.

In Figures 7 and (d), while keeping the other background parameters symmetric, we turned the external flows asymmetric, thus changing the phase speed limits posed by the external sound speeds by a different amount. This new asymmetry and the presence of a stronger downflow on the right-hand side led to a substantial change: forward-propagating body modes can no longer exist as trapped oscillations in this slab system, as their phase speed would exceed the external sound speed modified with the right-hand-side flow speed.

Since there is now a flow asymmetry in the system, Figure 7(d) shows similar properties to the results obtained in a fully asymmetric system (e.g., Figure 3). We prepared this figure for a fixed small slab width value, so that a wider range of KHI-unstable solutions could be showcased. The Alfvén Mach number on the left-hand side is still fixed as $M_{A1} = -0.1$, while it changes on the right-hand side as we move along the horizontal axis. As M_{A2} decreases from -0.1, first the forward-propagating body modes vanish, and then, at around $M_{A2} = -0.5$, the surface modes become unstable. Moving in the other direction, with increasing upflows on the right-hand side, it is backward-propagating body modes that vanish first, and then, at around $M_{A2} = 0.3$, the surface modes become unstable again. Comparing these instability limits, we might notice that the asymmetry in external Alfvén Mach numbers

$|M_{A1} - M_{A2}| \approx 0.4$ in both cases. This, however, also means that when we have an upflow and a downflow in the system, a smaller flow speed for both is enough to cause the appearance of an instability.

This effect of flow asymmetry is moderated by increasing the slab width, as Figures 7(c) and (d) show. While the process of having certain modes become leaky and others going unstable is qualitatively similar to the case we described in detail above, quantitatively, the wider our slab is, the greater the magnitude of the right-hand-side flow speed required for these changes becomes.

A different possibility for adding asymmetries to the symmetric slab system of Roberts II is to start by constructing a model for a static asymmetric slab, where $c_1 \neq c_2$ and $\rho_1 \neq \rho_2$. This type of slab geometry was investigated in detail by Allcock & Erdélyi (2017). Our Figure 7(e) depicts a series of solutions in this case, where each still image shows the phase speeds of trapped oscillations as a function of the slab width for a fixed value of symmetric flows $(M_{A1} = M_{A2} = M_{Ae})$. Depending on what this fixed flow speed is, as before, different modes are allowed, but the slab remains stable when $-1 < M_{Ae} < 1$. Complementing this figure, Figure 7(f) shows how the limits of instability change with each new fixed value of slab width.

Finally, we can add asymmetric external flows to an asymmetric static background, which is the case we discussed in detail throughout this paper and presented numerical results for in Figures 2 and 3, as well as Figures 4 and 5.

5. Conclusion

We constructed and studied a mathematical model of an isolated magnetic slab in an asymmetric environment with asymmetric external flows, generalizing the asymmetric magnetic slab model as initially described by Allcock & Erdélyi (2017) for the stationary case and by Barbulescu & Erdélyi (2018) for the steady case.

We have derived a dispersion relation for this model and provided an approximate (decoupled) version of it for small asymmetries. We found approximate solutions for the angular frequencies of the quasi-sausage and quasi-kink eigenmodes in thin and wide slabs, as well as hot and cold plasmas. To examine all possibilities, and to take a closer look at how exact the solutions are, we have also provided additional expressions derived from the full dispersion relation and compared our findings with numerical results.

Some of the most significant findings are that in every case the presence of bulk background flows broke the symmetry between the phase speeds of forward- and backward-propagating modes. The choice of external flow speed and asymmetry has also proven to have a marked influence on the phase speed of eigenmodes and thus changed the slab width and phase speed values for which trapped oscillations can be present. We have found that both the density asymmetry and flow asymmetry have a strong (first-order) effect on the angular frequencies of surface waves, and thus they also significantly change the limiting slab widths at which they would become leaky.

Furthermore, just like in a steady symmetric slab (Nakariakov & Roberts 1995) or in a steady asymmetric slab with an internal flow (Barbulescu & Erdélyi 2018), the KHI can be present in our asymmetric slab system too. We have conducted both an analytical and a numerical investigation of when this asymmetry

may set in for various choices of plasma and geometric parameters, as well as how the flow speeds and their asymmetry change this limit. We explored the possibilities of changing the slab width and the magnitude of the fixed left-hand-side flow while increasing or decreasing the right-hand-side flow (M_{A2}). Through this, we have found that, irrespective of the flow asymmetry, as a general tendency, thinner slabs tend to be unstable for a wider range of right-hand-side flow speeds. An additional future avenue of investigation could further expand this research and explore the connection of these parameters and results with changing the density asymmetry between the external regions, in addition to the shifting flow asymmetry.

For most of our numerical investigation, we used characteristic speed values that correspond to what we know so far about the photosphere—more specifically, about intergranular lanes and MBPs, as the latter are a prime candidate for applying the asymmetric slab model. Just as the KHI has been recently observed in the flank region of a CME by Foullon et al. (2011), it is our hope that new, high-resolution observations might soon be able to detect it in the region of small-scale phenomena such as MBPs as well, providing further opportunities for the study of MHD waves in slab-like configurations of the solar atmosphere.

ORCID iDs

Noémi Kinga Zsámberger ⓘ https://orcid.org/0000-0002-2822-129X
Róbert Erdélyi ⓘ https://orcid.org/0000-0003-3439-4127

References

Allcock, M., & Erdélyi, R. 2017, SoPh, 292, 35
Allcock, M., & Erdélyi, R. 2018, ApJ, 855, 90
Allcock, M., Shukhobodskaia, D., Zsámberger, N. K., & Erdélyi, R. 2019, FrASS, 6, 48
Andries, J., Tirry, W. J., & Goossens, M. 2000, ApJ, 531, 561
Barbulescu, M., & Erdélyi, R. 2018, SoPh, 293, 86
Blumen, W. 1970, JFM, 40, 769
Briand, C., & Solanki, S. K. 1998, A&A, 330, 1160
Danilovic, S., Schüssler, M., & Solanki, S. K. 2010, A&A, 509, A76
Edwin, P. M., & Roberts, B. 1982, SoPh, 76, 239
Felipe, T., Collados, M., Khomenko, E., et al. 2016, A&A, 596, A59
Foullon, C., Verwichte, E., Nakariakov, V. M., Nykyri, K., & Farrugia, C. J. 2011, ApJL, 729, L8
Habbal, S. R., Holzer, T. E., & Leer, E. 1979, in IAU Colloq. 44, Physics of Solar Prominences, ed. E. Jensen, P. Maltby, & F. Q. Orrall (Oslo: Institute of Theoretical Astrophysics), 228
Hurlburt, N. E., Alexander, D., & Rucklidge, A. M. 2002, ApJ, 577, 993
Jiang, R. L., Shibata, K., Isobe, H., & Fang, C. 2011, ApJL, 726, L16
Keys, P. H., Mathioudakis, M., Jess, D. B., et al. 2013, MNRAS, 428, 3220
Michalke, A. 1964, JFM, 19, 543
Nakariakov, V. M., & Roberts, B. 1995, SoPh, 159, 213
Ray, T. P. 1982, MNRAS, 198, 617
Roberts, B. 1981a, SoPh, 69, 27
Roberts, B. 1981b, SoPh, 69, 39
Ryutova, M. 2015, Physics of Magnetic Flux Tubes, Vol. 417, Astrophysics and Space Science Library (Berlin: Springer)
Shukhobodskaia, D., & Erdélyi, R. 2018, ApJ, 868, 128
Socas-Navarro, H., Martínez Pillet, V., & Lites, B. W. 2004, ApJ, 611, 1139
Somasundaram, K., Venkatraman, S., & Sengottuvel, M. P. 1999, PPCF, 41, 1421
Taroyan, Y., & Ruderman, M. S. 2011, SSRv, 158, 505
Terra-Homem, M., Erdélyi, R., & Ballai, I. 2003, SoPh, 217, 199
Tirry, W. J., Cadez, V. M., Erdelyi, R., & Goossens, M. 1998, A&A, 332, 786
Uchida, Y. 1968, SoPh, 4, 30
Wu, D., & Wang, D. 1991, MNRAS, 250, 760
Zaqarashvili, T. V., Lomineishvili, S., Leitner, P., et al. 2021, A&A, 649, A179
Zsámberger, N. K., Allcock, M., & Erdélyi, R. 2018, ApJ, 853, 136
Zsámberger, N. K., & Erdélyi, R. 2020, ApJ, 894, 123
Zsámberger, N. K., & Erdélyi, R. 2021, ApJ, 906, 122